IDH2 Mutations Define a Unique Subtype of Breast Cancer with Altered Nuclear Polarity

Sarah Chiang[1,*], **Britta Weigelt**[1,*], **Huei-Chi Wen**[1,*,§], **Fresia Pareja**[1], **Ashwini Raghavendra**[1], **Luciano G. Martelotto**[1], **Kathleen A. Burke**[1], **Thais Basili**[1], **Anqi Li**[1], **Felipe C. Geyer**[1], **Salvatore Piscuoglio**[1], **Charlotte K.Y. Ng**[1], **Achim A. Jungbluth**[1], **Jörg Balss**[2], **Stefan Pusch**[2], **Gabrielle M. Baker**[3], **Kimberly S. Cole**[4], **Andreas von Deimling**[2,5], **Julie M. Batten**[6], **Jonathan D. Marotti**[7], **Hwei-Choo Soh**[8], **Benjamin L. McCalip**[9], **Jonathan Serrano**[10], **Raymond S. Lim**[1], **Kalliopi P. Siziopikou**[11], **Song Lu**[12], **Xiaolong Liu**[13], **Tarek Hammour**[14], **Edi Brogi**[1], **Matija Snuderl**[10], **A. John Iafrate**[6,15], **Jorge S. Reis-Filho**[1], and **Stuart J. Schnitt**[15,16,†]

[1]Department of Pathology, Memorial Sloan Kettering Cancer Center, New York, NY, USA

[2]German Consortium of Translational Cancer Research (DKTK), Clinical Cooperation Unit Neuropathology, German Cancer Research Center (DKFZ), INF 280, Heidelberg, Germany

[3]Department of Pathology, University of Chicago, Chicago, IL, USA

[4]Department of Pathology, University of Iowa Hospital and Clinics, Iowa City, IA, USA

[5]Department of Neuropathology, Institute of Pathology, INF 224, Ruprecht-Karls-University Heidelberg, Heidelberg, Germany

[6]Department of Pathology, Massachusetts General Hospital, Boston, MA, USA

[7]Department of Pathology, Dartmouth-Hitchcock Medical Center, Lebanon, NH, USA

[8]Pathology North, North Shore Private Hospital, New South Wales, Australia

[9]Miami Valley Hospital, Dayton, OH, USA

[10]Department of Pathology, New York University Langone Medical Center and Medical School, New York, NY, USA

[11]Department of Pathology, Northwestern University Feinberg School of Medicine, Chicago, IL, USA

[12]Department of Pathology, Mon General Hospital, Morgantown, WV, USA

[13]ABQ Health Partners, Albuquerque, NM, USA

[14]Maine Medical Center, Portland, ME, USA

[15]Department of Pathology, Harvard Medical School, Boston, MA, USA

[†]Corresponding author: Department of Pathology, Beth Israel Deaconess Medical Center, 330 Brookline Ave, Boston, MA 02215, Phone: 617-667-4344, Fax: 617-975-5620, sschnitt@bidmc.harvard.edu.
[*]Equal contribution
[§]Current address: Department of Dermatology, Icahn School of Medicine at Mount Sinai, New York, NY, USA

[16]Department of Pathology, Beth Israel Deaconess Medical Center, Boston, MA, USA

Abstract

Solid papillary carcinoma with reverse polarity (SPCRP) is a rare breast cancer subtype with an obscure etiology. In this study, we sought to describe its unique histopathologic features and to identify the genetic alterations that underpin SPCRP using massively parallel whole-exome and targeted sequencing. The morphologic and immunohistochemical features of SPCRP support the invasive nature of this subtype. Ten of 13 (77%) SPCRPs harbored hotspot mutations at R172 of the isocitrate dehydrogenase *IDH2*, of which 8 of 10 displayed concurrent pathogenic mutations affecting *PIK3CA* or *PIK3R1*. One of the *IDH2* wild-type SPCRPs harbored a *TET2* Q548* truncating mutation coupled with a *PIK3CA* H1047R mutation. Functional studies demonstrated that *IDH2* and *PIK3CA* hotspot mutations are likely drivers of SPCRP, resulting in its reversed nuclear polarization phenotype. Our results offer a molecular definition of SPCRP as a distinct breast cancer subtype. Concurrent *IDH2* and *PIK3CA* mutations may help diagnose SPCRP and possibly direct effective treatment.

Keywords

INTRODUCTION

Breast cancer is a heterogeneous disease at the clinical, morphologic, and genetic level (1-3). The current World Health Organization (WHO) classification recognizes 21 histologic types (1), but few have been found to harbor specific genetic alterations, such as *CDH1* alterations in invasive lobular carcinoma (4) and recurrent *ETV6-NTRK3* and *MYB-NFIB* fusion genes in secretory and adenoid cystic carcinomas, respectively (5-7). Additional rare breast cancers with distinctive morphologic features also exist, but have not yet been included in the WHO classification. One such malignancy has been described as "breast tumor resembling the tall cell variant of papillary thyroid carcinoma (PTC)" (8,9), which has a unique histologic appearance consisting of solid, circumscribed nodules of epithelial cells, many of which have fibrovascular cores, resulting in a solid papillary growth pattern. Thirteen such tumors have been reported to date (8,9), of which approximately half lack estrogen (ER) and progesterone receptor (PR) expression, and all lack HER2 overexpression (8,9). These tumors are generally associated with a favorable prognosis (8,9), however two of 13 patients have been reported to develop metastatic disease, one to an intra-mammary lymph node and another to the bone (8,9).

Although these tumors have some histologic similarities to PTC, they consistently lack expression of thyroid-specific markers, including TTF-1 and thyroglobulin (8,9). *RET* rearrangements and *BRAF* exon 15 mutations commonly found in PTC have also not been detected in these tumors (9). Given the morphologic overlap with other papillary lesions of the breast and lack of immunohistochemical and genetic evidence of an association with PTC, it has recently been suggested that these neoplasms should be considered morphologic variants of papillary breast carcinoma(9,10).

In this study, we sought to characterize the morphologic and genetic landscape of this rare and morphologically unusual breast tumor and determine whether it represents a distinct subtype of breast cancer underpinned by disease-specific genetic alterations. To this end, we performed an extensive immunohistochemical characterization and whole exome (WES), targeted, and Sanger sequencing of 13 previously unreported tumors. We found that 10 of 13 (77%) tumors harbored R172 *IDH2* mutations, of which eight had a concurrent pathogenic mutation affecting PI3K pathway canonical genes (i.e. six *PIK3CA* hotspot mutations and two *PIK3R1* likely pathogenic mutations). In addition, a *PIK3CA*-mutant but *IDH2*-wild-type tumor was found to harbor a *TET2* Q548* truncating mutation. Functional studies using nonmalignant breast epithelial cells demonstrated that *IDH2* and *PIK3CA* mutations constitute likely drivers of this tumor and contribute to its characteristic phenotype. Because of their unique histologic and genetic properties, we redefine these tumors here as a discrete subtype of breast carcinoma: solid papillary carcinoma with reverse polarity (SPCRP).

MATERIALS AND METHODS

Patient selection

Between 2005 and 2014, 13 SPCRPs were identified by two of the authors (S.J. Schnitt and E. Brogi) on the Breast Pathology Consultation (11 cases) or Breast Pathology (1 case) Services at Beth Israel Deaconess Medical Center (Boston, MA) and the Breast Pathology Consultation Service (1 case) at Memorial Sloan Kettering Cancer Center (MSKCC; New York, NY). Hematoxylin-and-eosin-stained sections were reviewed to delineate the morphologic features of these lesions. Available clinical data were reviewed for demographics, presentation, clinical and family history, treatment, and outcome. The study was approved by the Institutional Review Boards from the respective authors' institutions, and all samples were anonymized prior to analysis.

Immunohistochemistry and Western blotting

Primary antibodies for immunohistochemistry (IHC) were as follows: calponin, smooth muscle myosin-heavy chain (SMMHC), p63, AE1/AE3, cytokeratin (CK) 7, CK5/6, CK34βE12, ER, PR, androgen receptor (AR), HER2, mammaglobin, H3K27me3, gross cystic disease fluid protein-15 GCDFP-15, TTF-1, thyroglobulin, E-cadherin, and MUC1 (Supplementary Table S1). For H3K27me3, we semi-quantitatively assessed its nuclear expression using the H-score system as previously described (11); 500 nuclei were counted per case.

Standard Western blotting was performed as previously described (12) using primary antibodies against IDH2 and H3K9me3 (Abcam); phospho-Rb (S807/811), Rb (4H1), histone H3 (D1H2), and α-tubulin (DM1A) (Cell Signaling Technology); H3K27me3 (EMD Millipore) and E-cadherin (BD Biosciences). Secondary conjugated IRDye 680RD/800CW antibodies (LI-COR Biosciences) were used. Detection and quantification were performed using the Image Studio Software from LI-COR (LI-COR Biosciences) (13,14).

Whole exome and targeted massively parallel sequencing

Eight μm-thick representative formalin-fixed paraffin-embedded (FFPE) tumor and normal tissue sections from two SPCRPs (cases 10 and 13), and tumor sections from two SPCRPs (cases 5 and 11) were stained with nuclear fast red and microdissected using a sterile needle under a stereomicroscope (Olympus SZ61), to ensure >80% tumor cell content and that normal tissue was devoid of neoplastic cells as previously described (5,14). DNA was extracted from microdissected tumor and normal samples using the DNeasy Blood and Tissue Kit (Qiagen) following the manufacturer's guidelines. Tumor and matched germline DNA from SPCRP10 and SPCRP13 were subjected to WES on a Illumina HiSeq2000 at the Integrated Genomics Operation (IGO) at MSKCC (14), and tumor DNA from SPCRP5 and SPCRP11 to Memorial Sloan Kettering-Integrated Mutation Profiling of Actionable Cancer Targets (MSK-IMPACT) sequencing assay (15) targeting all exons and selected regulatory regions and introns of 410 key cancer genes on a Illumina HiSeq2500 (16). Massively parallel sequencing analysis was performed as previously described (Supplementary Methods; refs. 16, 17). WES and MSK-IMPACT data have been submitted to SRA under the accessions SRP066429 and SRP066430, respectively.

SNaPshot genotyping

Representative FFPE sections of each case were reviewed to select the most appropriate tumor-enriched area for analysis. Tumor tissue was manually microdissected from serial 5-μm-thick unstained sections. Total nucleic acid was extracted from FFPE tumor tissue using a modified FormaPure system (Agencourt Bioscience Corporation) as previously described (18). Genotyping analysis of specific mutations in 22 clinically relevant cancer genes (Supplementary Table S2), was performed on six SPCRPs (cases 2, 4, 7-9, and 12) for which insufficient material for massively parallel sequencing was available using a custom Applied Biosystem (ABI) Prism SNaPshot Multiplex platform, as previously reported (18).

Sanger sequencing

For three cases (SPCRP1, 3 and 6) with very limited tissue availability, DNA was subjected to PCR amplification using primer sets encompassing the *IDH2* R140 and R172 hotspot residues and the *PIK3CA* E542/545 and H1047 hotspot residues (Supplementary Table S3), followed by standard Sanger sequencing as previously described (14). All analyses were performed in duplicate. Sequences of the forward and reverse strands were analyzed using MacVector software (MacVector, Inc; ref. 14).

Methylation profiling

Methylation profiling was performed using the Infinium MethylationEPIC Kit (Illumina). DNA samples from five *IDH2*-mutant SPCRPs (cases 3-5, 7, and 9), one *TET2*-mutant SPCRP (case 11) and two invasive ductal carcinomas of no special type (IDCs, one ER-positive/HER2-negative and one ER-negative/HER2-negative) were bisulfite-converted using the EZ-96 DNA Methylation Kit (Zymo Research), restored using the Illumina Infinium HD FFPE DNA Restore Kit, and whole-genome amplified (Supplementary Methods). The BeadChips were scanned, and the raw data files containing the fluorescence

intensity data for each probe were generated. Data analysis was performed using RnBeads (Supplementary Methods; ref. 19).

DNA transfections and analysis of transgene expression

The human *IDH2* (NM_002168) cDNA ORF clone pCMV6-IDH2::Myc-DDK was purchased from Origene (RC201152), and the R172S mutation introduced using the Q5 Site-Directed Mutagenesis Kit (New England Biolabs) following the manufacturer's recommendations. The presence of the correct mutation was confirmed by Sanger sequencing (for primers, see Supplementary Table S3). *IDH2* wild-type and mutant (R172S) open reading frames were cloned into the pCMV6-TagRFP or pCMV6-TagGFP vector to generate pCMV6-IDH2::TagRFP/GFP and pCMV6-IDH2(R172S)::TagRFP/GFP plasmids, respectively, as previously described (13,14). Transfections of plasmids were performed using Lipofectamine 3000 reagent according to the manufacturer's guidelines(13). IDH2 and IDH2 R172S expression was verified by immunofluorescence-based mitochondrial co-localization using MitoTracker staining (Thermo Fisher Scientific), quantitative RT-PCR and whole cell lysate protein detection.

Quantitative RT-PCR (qRT-PCR)

TaqMan quantitative RT-PCR (qRT-PCR; Life Technologies) was performed for *IDH2* (Hs00158033_m1), Twist1 (Hs01675818_s1), SNAI1 (Hs00195591_m1), SNAI2 (Hs00161904_m1), FN1 (Hs01549976_m1), and using GAPDH (Hs99999905_m1) for expression assay normalization, as previously described (5,20).

2-hydroxyglutarate assay of tissue samples and cell lines

Ten serial 10 μm-thick representative tumor sections were obtained of SPCRP12 and five IDCs, the latter identified in the pathology database at Massachusetts General Hospital and diagnosis confirmed. Tumors were manually microdissected. 2-Hydroxyglutarate (2HG) was analyzed in lysates from these samples using gas chromatography/mass spectrometry, as previously described (21).

Parental MCF10A (MCF10A^P) and MCF10A *PIK3CA* H1047R (MCF10A^{H1047R}) knock-in cells were obtained from Horizon in December 2014. The identities of the cell lines were confirmed by short tandem repeat profiling using the GenePrint 10 System (Promega) in the IGO at MSKCC three months after receipt. In addition, cells were tested for mycoplasma infection using a PCR-based test (ATCC). Confluent cells (MCF10A^P and MCF10A^{H1047R}, expressing vector control, *IDH2* wild-type, or *IDH2* R172S plasmids) were collected from 6-well plates, and 2HG detection was performed in conditioned media and in cell lysates, as previously reported (22; Supplementary Methods). Fluorometric detection was carried out in triplicate with excitation at 540 nm and emission of 610 nm (Victor X4 Multimode Plate Reader, Supplementary Methods).

Cell proliferation and cell migration assays

MCF10A^P and MCF10^{H1047R} cells were transfected with pCMV6-TagRFP empty vector, pCMV6-TagRFP-IDH2^{WT} or pCMV6-TagRFP-IDH2^{R172S} using Lipofectamine 3000 (Invitrogen) as per manufacturer's instructions. After 48 hours, cells were trypsinized,

collected and RFP-, RFP-IDH2^{WT}, and RFP-IDH2^{R172S}, expressing cells selected by flow cytometry sorting. For proliferation, the sorted cells were seeded in 96, well plates (1,000 cells/well) in triplicates. Cell growth was assessed every 24 h by CellTiter-Blue assay (Promega) and fluorometric detection performed with 560 nm excitation and 590 nm emission using a VICTOR X4 Multilabel Plate Reader (PerkinElmer). For migration, cells were starved for 16 h in 2% horse serum DMEM/F12 medium without EGF. Cells were seeded (0.5×10^5) in the upper compartment of a 24-well transwell insert (8 μm pore membranes; Corning) and allowed to adhere and migrate at 37°C towards 10% horse serum and EGF containing DMEM/F12 medium for 16 h. Cells adherent to the upper side of the transwell membrane were removed, and cells on the inferior side of were fixed in 4% paraformaldehyde (PFA), permeabilized (0.5% Triton X-100 in PBS), and stained with crystal violet (0.3%). Transwell membranes were imaged (EVOS XL Imaging System, Life Technologies) and analyzed by ImageJ.

3D cell culture

3D cell culture assays were carried out as previously described (13,14,23,24). Phase-contrast images of acinar structures were acquired after six days (EVOS XL Imaging System). Size (mm^3) of 3D acinar structures was determined using Fiji (Image J software) to define Feret diameter (D) and minimum Feret diameter (d) and applying the formula (D $\times$ d^2)/2=acini volume. Immunofluorescent staining of 3D acini (12 days) was performed as previously described (24). The structures were fixed in 4% PFA and permeabilized (0.5% Triton X-100 in PBS), stained using antibodies against GM130 (D6B1) and E-cadherin (Cell Signaling Technology), and Alexa Fluor–conjugated secondary antibodies and ProLong Gold antifade reagent with DAPI (Life Technologies), and imaged by confocal analyses ([Leica SP5 DM, including an ultraviolet (UV) diode (405 nm), argon laser(458, 476, 488, and 514 nm), 543-nm HeNe laser, and 633-nm HeNe laser). Polarity assessment was performed with the observer blinded to the genotype of the cell line being analyzed, with apical polarity defined as nuclei at the basal pole (near the periphery of the acini) and Golgi apparatus facing upwards (towards the lumen), and reverse polarity as nuclei at the apical pole (towards to the lumen) and Golgi apparatus facing away from the lumen (near the periphery of the acini). A minimum of 100 abluminallylocated cells were counted per experimental condition in each cell line.

Oxidative stress cell viability assay

A cell viability assay for the assessment of oxidative stress was performed basically as previously described (25). Vector-, IDH2- or IDH2 R172S-expressing MCF10A^P and MCF10A^{H1047R} were grown overnight on a 96-well plate at a density of 1×10^4 cells/well, treated with 1 mmol/L hydrogen peroxide (H$_2$O$_2$) in serum-free medium for 48 hours at 37°C, and cell viability was assessed using CellTiter-Blue as described above and reported as compared to absorbance measured in untreated control cells. Fluorometric detection was carried out in triplicate in two independent experiments.

RESULTS

Clinicopathologic characteristics of SPCRP

SPCRP has a very distinctive histologic appearance that allowed us to identify a series of 13 such tumors from our consultation and institutional files. They consisted of solid, circumscribed nodules of columnar epithelial cells, some exhibiting a geographic, jigsaw-like growth pattern (Fig. 1A-C). Many nodules contained fibrovascular cores with foamy histiocytes and a double-layered epithelium without a clear lumen, resulting in a solid papillary appearance (Fig. 1B). The cells in many nodules appeared back-to-back and, in particular, the nuclei were present at the apical rather than basal pole of the cells, creating the impression of reverse polarization (Fig. 1C).

In all cases, all tumor nodules lacked a surrounding myoepithelial cell layer as assessed by immunohistochemical analysis for p63 (Fig. 1E), calponin, and SMMHC, supporting the invasive nature of these lesions. Tumor cells showed strong cytoplasmic expression of low-molecular weight CK7, but also strongly expressed high-molecular weight/basal CK5/6 (Fig. 1D) and CK34βE12. GCDFP-15 and mammaglobin expression were detected in 62% and 58% of cases, respectively, supporting the breast origin of the tumors, whereas thyroglobulin and TTF-1 were negative in all tumors, excluding metastases of a thyroid carcinoma. In 62% of cases, tumor cells were entirely ER-negative (Fig. 1F); ER expression was seen in 1 to 10% of cells in the remaining tumors. PR expression was seen in 15% of cases, and all cases studied were negative for HER2 protein overexpression. AR was focally positive in only one case. In two cases studied, the Ki67 proliferation rate was low (<5%). E-cadherin staining revealed strong lateral membrane expression with absent apical or basal expression (Fig. 1G), suggesting that the epithelium is polarized. MUC1 staining, which highlights the apical membranes of columnar epithelial cells, was identified at the end of the cell closest to the nucleus, indicating that the nuclei were in an abnormal location (apical rather than basal) and creating the impression of reversed cell polarity (Fig. 1H). Clinical data are summarized in Table 1.

SPCRP harbors *IDH2* hotspot mutations and mutations affecting PI3K pathway canonical genes

Two SPCRPs (cases 10 and 13), for which sufficient tumor and normal DNA samples were available, and two SPCRPs (cases 5 and 11) with sufficient tumor DNA were subjected to WES and the MSK-IMPACT sequencing assay(15), respectively. In cases subjected to WES (cases 10 and 13), the median sequencing depth of coverage was 127x (range 111-212x), and 45 and 24 nonsynonymous somatic mutations were identified (Supplementary Tables S4 and S5). Cases 5 and 11, subjected to MSK-IMPACT sequencing at a coverage of 734x and 573x, respectively, were found to harbor eight and 26 non-synonymous somatic mutations, respectively (Supplementary Tables S4 and S5). Sequencing analysis revealed that these three cases harbored somatic single nucleotide variants (SNV) affecting the R172 residue in the substrate-binding pocket of the isocitrate dehydrogenase 2 (NADP+), mitochondrial (*IDH2*) gene (Fig. 2A; Supplementary Table S5), the same *IDH2* codon targeted by recurrent hotspot mutations in glioma, acute myeloid leukemia (AML), cholangiocarcinoma, and chondrosarcoma (26). In SPCRP11, which lacked an *IDH2* somatic mutation, a *TET2*

Q548* truncating mutation was detected. We also identified mutations affecting canonical genes of the PI3K/AKT/mTOR pathway in all four SPCRPs, with two cases harboring *PIK3R1* frameshift mutations and two cases harboring *PIK3CA* somatic mutations (Fig. 2A; Supplementary Table S5). No other recurrent somatic mutations were found. To validate these findings, we subjected DNA derived from an additional six SPCRPs (cases 2, 4, 7-9, and 12) to SNaPshot profiling assessing mutations in 22 cancer genes (Supplementary Table S2) and from three SPCRPs (cases 1, 3, and 6) to *IDH2* and *PIK3CA* hotspot Sanger sequencing (Fig. S1, Supplementary Table S3), which confirmed the presence of *IDH2* R172 hotspot mutations in seven cases (70%), and *PIK3CA* H1047R and E542K hotspot mutations in six cases and one case (78%), respectively. No other hotspot mutations were identified in the SPCRPs subjected to SNaPshot profiling. In total, 10 of 13 (77%) SPCRPs analyzed here harbored an *IDH2* R172 mutation, of which five had a concurrent *PIK3CA* H1047R hotspot mutation, one a concurrent *PIK3CA* C420R mutation, and two a concurrent *PIK3R1* frameshift mutation (Fig. 2A). Given that one of the *IDH2* wild-type SPCRPs harbored a truncating mutation in *TET2*, which encodes for an α-ketoglutarate (αKG)-dependent enzyme that catalyzes cytosine 5-hydroxymethylation resulting in demethylation of DNA (27), we sought to define whether the *IDH2* wild-type cases SPCRP1 and SPCRP6 would also harbor mutations affecting this gene; however both were found to be *TET2* wild-type. No histologic differences were observed among the *IDH2*-mutant, *TET2*-mutant and *IDH2*/*TET2* wild-type SPCRPs.

To date, *IDH2* mutations have not been described in breast cancer, and a re-analysis of breast cancers reported by The Cancer Genome Atlas (TCGA) revealed that only one of the 971 invasive ductal and invasive lobular carcinomas harbored an *IDH2* mutation, however affecting a different codon (E345K, Fig. 2B; www.cBioPortal.org, accessed on November 30, 2015; Fig. 2B; refs. 4, 28). Taken together, our results indicate that SPCRPs are uniquely characterized by highly recurrent *IDH2* R172 hotspot mutations often in combination with mutations affecting PI3K pathway canonical genes, in particular in the form of *PIK3CA* H1047R hotspot mutations, and suggest that at least in a subset of SPCRPs lacking *IDH2* mutations, somatic genetic alteration affecting *TET2* may be present. These observations suggest that SPCRPs may constitute an example of a convergent phenotype stemming from alterations of genes leading to similar epigenetic defects and potentially function genetically in the same pathway (26,29), as *IDH1*/*IDH2* mutations inhibit *TET2* function and are mutually exclusive with *TET2* mutations in hematological malignancies (30).

IDH2 and *PIK3CA* mutations constitute likely drivers of SPCRP

IDH2 hotspot mutations are enzymatic gain-of-function alterations that lead to an increased conversion of αKG to 2-hydroxyglutarate (2HG). Increased levels of 2HG result in hypermethylation of epigenetic targets and a subsequent block in cellular differentiation (31,32). We first sought to define whether *IDH2* mutations result in accumulation of 2HG oncometabolite in SPCRP as reported in glioblastoma (33) and AML (34) harboring this mutation. We measured intratumoral 2HG by gas chromatography/mass spectrometry in one *IDH2*-mutant SPCRP (case 12), where adequately preserved tissue was available, and five *IDH*-wild-type IDCs with available material. The SPCRP harboring the *IDH2* R172T mutation demonstrated an elevated 2HG level of 49.36 pmol/μg protein (Fig. 2C). In four

IDH2-mutant SPCRPs, tissue samples were inadequate and rendered uninterpretable levels of 2HG (data not shown). All five *IDH2*-wild-type IDCs harbored undetectable levels of 2HG (Fig. 2C). We next sought to define levels of methylation in *IDH2*/*TET2*-mutant SPCRPs, for which DNA samples were available. Genome-wide DNA methylation analysis using the Illumina Infinium MethylationEPIC BeadChip revealed that *IDH2*/*TET2*-mutant SPCRPs showed a genome-wide hypermethylation profile as compared to *IDH2* wild-type IDCs, consistent with the hypermethylation profile reported in *IDH1*/*IDH2*-mutant cancers (Fig. 2D, Supplementary Fig. S2; refs. 30, 35). In fact, hierarchical clustering revealed that *IDH2*/*TET2*-mutant SPCRPs clustered together based on their methylation profile, and separate from the two *IDH2*/*TET2* wild-type IDCs analyzed (Fig. 2D). Finally, the protein expression levels of H3K27me3 were assessed by IHC in four *IDH2*-mutant SPCRPs for which adequate histologic sections were available, and in four IDCs (two ER-positive/HER2-negative and two ER-negative/HER2-negative). Compared to *IDH2* wild-type IDCs, *IDH2*-mutant SPCRPs displayed significantly higher levels of trimethylation of H3K27 (K3K27me3, p=0.029, Mann-Whitney U test; Fig. 2E), consistent with the results reported in *IDH*-mutant gliomas (31).

We next tested the functional impact of the *IDH2* R172S mutation on the growth and phenotype of nonmalignant breast epithelial cells and investigated potential epistatic interactions between *IDH2* R172S and the most frequent *PIK3CA* (H1047R) mutations concurrently detected in SPCRPs. We employed the MCF10A model system, including parental MCF10A cells and MCF10A cells harboring a stable knock-in of the *PIK3CA* H1047R mutation. As expected, forced expression of wild-type IDH2 (IDH2^{WT}) and R172S mutant IDH2 (IDH2^{R172S}) in parental MCF10A cells (MCF10A^P) and in *PIK3CA* H1047R mutant MCF10A cells (MCF10A^{H1047R}) resulted in increased IDH2 mRNA expression (Supplementary Fig. S3A) and IDH2 protein mitochondrial localization (Supplementary Fig. S3B). When expressed at similar protein levels, IDH2^{R172S} resulted in significantly higher neomorphic enzymatic activity than IDH2^{WT} based on the analysis of the production and secretion of 2HG, regardless of the presence of the H1047R *PIK3CA* mutation (Fig. 3A).

IDH1 and *IDH2* mutations have been shown to constitute drivers of glioma (36,37), AML (34,38), and spindle cell hemangioma (39,40) among others, resulting in a differentiation block and tumorigenesis (31,32). Although in our transient transfection system, no statistically significant differences in the expression levels of H3K27 and H3K9 trimethylation were observed upon forced expression of IDH2^{WT} or IDH2^{R172S} as compared to cells expressing empty vector (Supplementary Fig. S4), expression of IDH2^{R172S} expression resulted in changes in expression of cell-cycle and epithelial-mesenchymal transition (EMT) markers in the nonmalignant breast epithelial cells, MCF10A. Forced expression of IDH2^{R172S} in MCF10A^{H1047R} cells led to significantly increased phosphorylation of RB1 protein compared with empty vector, as detected by immunoblot (Fig. 3B). Consistent with these observations, we observed a significant increase in cell growth upon forced expression of IDH2^{WT} and IDH2^{R172S} in MCF10A^{H1047R} cells (Fig. 4A), as well as a significant increase in migration of MCF10A^{WT} and MCF10A^{H1047R} cells expressing R172S-mutant IDH2 (Fig. 4B). Furthermore, we observed that forced expression of IDH2^{WT} and IDH2^{R172S} led to a reduction of E-cadherin protein expression in

MCF10A^{H1047R} cells (Fig. 3B) and resulted in significantly increased levels of EMT markers in MCF10A cells harboring wild-type or H1047R-mutant *PIK3CA* (Fig. 4C).

Given that cancer cells can avoid cell death by inhibiting the initial deleterious effects of oxidative stress (25,41), we sought to define the impact of IDH2^{R172S} on the viability of nonmalignant breast epithelial cells. In MCF10A^{P} cells treated with exogenous H_2O_2, forced expression of wild-type, but not mutant IDH2 displayed a higher viability than empty vector expression (Fig. 4D). In H_2O_2-treated MCF10A^{H1047R} cells, however, forced expression of both wild-type and mutant IDH2 resulted in increased viability compared with the empty vector control (Fig. 4D). These results suggest that IDH2^{R172S} may protect against reactive oxygen species (ROS) in nonmalignant breast epithelial cells, consistent with observations described previously for IDH1 and IDH2 in other nonneoplastic tissue types (25,41).

We next sought to define the impact of IDH2^{R172S} on the growth and glandular architecture of MCF10A cells grown in a 3D model system, which has been previously employed to assess the oncogenic properties of somatic mutations (13,23,42). Forced expression of IDH2^{R172S} in MCF10A^{P} and MCF10A^{H1047R} cells resulted in acinar structures that were significantly larger than those observed in MCF10A cells transfected with empty vector or IDH2^{WT} (Fig. 5A), a phenotype that previously reported to be elicited by the expression of *bona fide* oncoproteins in this model system (13,23,42). In fact, IDH2^{R172S} expression in MCF10A^{H1047R} cells led to the formation of anastomosing solid cell nests/ cell nodules (Fig. 5A and Supplementary Fig. S5). Consistent with the reverse polarization observed in the primary tumors, IDH2^{R172S} expression in MCF10A cells grown in the 3D system also resulted in an increase in cells displaying a reversed nuclear polarity, as defined by expression of adhesion molecule E-cadherin (CDH1) and apical Golgi marker GM130. This reversed nuclear polarity phenotype was particularly evident in MCF10A^{H1047R} cells expressing IDH2^{R172S} (Fig. 5B). Taken together, our data provide evidence that *IDH2* R172S and *PIK3CA* H1047R hotspot mutations constitute likely drivers of SPRCP, and that together these somatic genetic alterations are likely sufficient, but not necessarily required, to cause its unusual reverse polarization phenotype.

DISCUSSION

Here we characterize the morphologic, immunohistochemical and genomic profile of SPCRP, a rare and histologically distinct subtype of invasive breast carcinoma. Through whole exome and targeted massively parallel sequencing analysis, we have identified *IDH2* hotspot and *TET2* truncating mutations in 77% and 8% of these cases, respectively. In fact, SPCRPs may constitute an example of a convergent phenotype as *IDH2* and *TET2* mutations lead to similar epigenetic defects (26,29). This is the first report of *IDH2* hotspot mutations detected in breast cancer, expanding the spectrum of solid tumors and hematologic malignancies in which *IDH* mutations may drive tumorigenesis(43). The high frequency of *IDH2* mutations found in SPCRP highlights the association between genotype and the unique tumor morphology (29). In addition, mutations affecting canonical genes of the PI3K pathway were found in 85% of SPCRPs, including 54% harboring *PIK3CA* H1047R, a common genetic alteration in breast cancer that may be enriched in this subset of tumors (44).

A striking feature of SPCRP is the unique epithelial morphology of a double-layer of columnar cells with apical nuclei. Absence of expression of E-cadherin, a protein known to play an important role in cell polarity, in apical and/or basal membranes combined with strong MUC1 staining of apical membranes indicate that the cells are indeed polarized. The presence of nuclei near the apical membrane indicates reverse nuclear polarization, and loss of apical polarity were also observed in our cell line models, in particular in cells expressing mutant forms of *IDH2* and *PIK3CA*, suggesting that this phenotype may result from epistatic interactions between mutations affecting these genes. Although our findings provide a novel example of a genotypic-phenotypic correlation in breast cancer, further analyses are required to define the genetic basis of the reverse polarity in SPCRPs lacking *IDH2, TET2* and/or PI3K pathway gene mutations.

The mechanism by which *IDH1* or *IDH2* mutations cause human cancer remains to be fully elucidated. It has been found, however, that these alterations lead to a gain-of-function enzymatic activity that allows NADPH-dependent reduction of αKG to 2HG within tumor cells (33,34), which inhibits αKG-dependent dioxygenases and alters genome-wide histone and DNA methylation, cell differentiation and survival, and extracellular matrix maturation (26,31,45). High 2HG concentrations disrupt *TET2* catalytic function and prevent hydroxylation of 5-methylcytosine, resulting in attenuated *TET2*-dependent demethylation of DNA (30,45). Akin to *IDH*-mutant glioma, AML and common forms of breast carcinoma harboring *IDH1* mutations (33,34,46), we found high concentrations of intratumoral 2HG in the *IDH2*-mutant SPCRP successfully tested; the use of archival material makes this analysis challenging as formalin fixation and paraffin embedding may lead to oncometabolite loss (21). In addition, we observed global DNA hypermethylation and H3K27 trimethylation in *IDH2*/*TET2*–mutant SPCRPs as compared to *IDH2* wild-type IDCs, consistent with those reported in *IDH1*/*IDH2*-mutant cancers (26,30,31,35). IDH1 and IDH2 have been described previously to protect cells from ROS (25,41). We observed that IDH2^{R172S} provided ROS protection in MCF10A^{H1047R} but not in MCF10A^{P} cells. Further studies are warranted to assess the potential mechanistic interaction between mutant *IDH2*, mutant PI3K and ROS, in particular because intracellular ROS levels have been reported to affect the PI3K pathway (for a review, see ref. 47).

IDH2 mutations in SPCRP may serve as a novel target for therapeutic intervention in breast cancer. Acquired enzymatic activity resulting in 2HG accumulation is specific to tumor cells, making mutant-specific small molecule inhibitors an attractive alternative to chemotherapy regimens with systemic toxic effects. *IDH2* inhibitors have now entered Phase 1 clinical trials for the treatment of AML with favorable safety profiles and durable clinical activity (48). Clinical benefit in the solid tumor patient population has yet to be demonstrated.

This study has important limitations. First, owing to the rarity of SPCRP, we studied 13 *bona fide* cases of this entity. Despite the small sample size, this is the largest collection of SPCRPs reported to date. Second, most samples were individual contributions from different institutions; hence we were unable to perform a survival analysis to ascertain the impact of *IDH2* mutations on the outcome of SPCRP. Importantly, given that none of the patients included in this study developed a distant relapse during the follow-up period available and

Author Manuscript

Author Manuscript

Author Manuscript

Author Manuscript

that less than 25% of SPCRPs lack *IDH2* hotspot mutations, it is unlikely that these mutations would be of prognostic significance. Third, we were unable to identify the driver genetic alterations in two SPCRPs lacking *IDH2* hotspot and *TET2* mutations by Sanger sequencing; however, due to the rarity of *IDH2/TET2*-wild-type SPCRPs and the limited material available from the cases analyzed, we were unable to sequence the entire coding region of *TET2* in the remaining cases. Further studies of *IDH2* wild-type SPCRPs are warranted.

Despite these limitations, here we have identified somatic *IDH2* hotspot mutations or *TET2* mutations in conjunction with mutations affecting PI3K pathway genes in SPCRP, validating this rare breast cancer as a unique clinico-pathologic entity underpinned by a distinctive constellation of somatic mutations. Detection of *IDH2* mutations may serve as an ancillary marker for the diagnosis of SPCRP. Broad-base genetic profiling in breast cancer patients who develop progressive disease with this tumor type may efficiently identify those eligible for clinical trials for *IDH* inhibition.

Supplementary Material

Refer to Web version on PubMed Central for supplementary material.

Acknowledgments

References

1. Lakhani, SR., Ellis, IO., Schnitt, SJ., Tan, PH., van de Vijver, MJ. WHO Classification of Tumours of the Breast. Lyon: IARC; 2012.

2. Ng CK, Schultheis AM, Bidard FC, Weigelt B, Reis-Filho JS. Breast cancer genomics from microarrays to massively parallel sequencing: paradigms and new insights. J Natl Cancer Inst. 2015; 107

3. Weigelt B, Reis-Filho JS. Histological and molecular types of breast cancer: is there a unifying taxonomy? Nat Rev Clin Oncol. 2009; 6:718–30. [PubMed: 19942925]

4. Ciriello G, Gatza ML, Beck AH, Wilkerson MD, Rhie SK, Pastore A, et al. Comprehensive Molecular Portraits of Invasive Lobular Breast Cancer. Cell. 2015; 163:506–19. [PubMed: 26451490]

5. Martelotto LG, De Filippo MR, Ng CK, Natrajan R, Fuhrmann L, Cyrta J, et al. Genomic landscape of adenoid cystic carcinoma of the breast. J Pathol. 2015; 237:179–89. [PubMed: 26095796]

6. Persson M, Andren Y, Mark J, Horlings HM, Persson F, Stenman G. Recurrent fusion of MYB and NFIB transcription factor genes in carcinomas of the breast and head and neck. Proc Natl Acad Sci U S A. 2009; 106:18740–4. [PubMed: 19841262]

7. Tognon C, Knezevich SR, Huntsman D, Roskelley CD, Melnyk N, Mathers JA, et al. Expression of the ETV6-NTRK3 gene fusion as a primary event in human secretory breast carcinoma. Cancer Cell. 2002; 2:367–76. [PubMed: 12450792]

8. Colella R, Guerriero A, Giansanti M, Sidoni A, Bellezza G. An additional case of breast tumor resembling the tall cell variant of papillary thyroid carcinoma. Int J Surg Pathol. 2015; 23:217–20. [PubMed: 24868004]

9. Masood S, Davis C, Kubik MJ. Changing the term "breast tumor resembling the tall cell variant of papillary thyroid carcinoma" to "tall cell variant of papillary breast carcinoma". Adv Anat Pathol. 2012; 19:108–10. [PubMed: 22313838]

10. Hameed O, Perry A, Banerjee R, Zhu X, Pfeifer JD. Papillary carcinoma of the breast lacks evidence of RET rearrangements despite morphological similarities to papillary thyroid carcinoma. Mod Pathol. 2009; 22:1236–42. [PubMed: 19543246]

11. Budwit-Novotny DA, McCarty KS, Cox EB, Soper JT, Mutch DG, Creasman WT, et al. Immunohistochemical analyses of estrogen receptor in endometrial adenocarcinoma using a monoclonal antibody. Cancer Res. 1986; 46:5419–25. [PubMed: 3756890]

12. Weigelt B, Warne PH, Downward J. PIK3CA mutation, but not PTEN loss of function, determines the sensitivity of breast cancer cells to mTOR inhibitory drugs. Oncogene. 2011; 30:3222–33. [PubMed: 21358673]

13. Ng CK, Martelotto LG, Gauthier A, Wen HC, Piscuoglio S, Lim RS, et al. Intra-tumor genetic heterogeneity and alternative driver genetic alterations in breast cancers with heterogeneous HER2 gene amplification. Genome Biol. 2015; 16:107. [PubMed: 25994018]

14. Weinreb I, Piscuoglio S, Martelotto LG, Waggott D, Ng CK, Perez-Ordonez B, et al. Hotspot activating PRKD1 somatic mutations in polymorphous low-grade adenocarcinomas of the salivary glands. Nat Genet. 2014; 46:1166–9. [PubMed: 25240283]

15. Cheng DT, Mitchell TN, Zehir A, Shah RH, Benayed R, Syed A, et al. Memorial Sloan Kettering-Integrated Mutation Profiling of Actionable Cancer Targets (MSK-IMPACT): A Hybridization Capture-Based Next-Generation Sequencing Clinical Assay for Solid Tumor Molecular Oncology. J Mol Diagn. 2015; 17:251–64. [PubMed: 25801821]

16. Piscuoglio S, Ng CK, Murray M, Burke KA, Edelweiss M, Geyer FC, et al. Massively parallel sequencing of phyllodes tumours of the breast reveals actionable mutations, and TERT promoter hotspot mutations and TERT gene amplification as likely drivers of progression. J Pathol. 2016; 238:508–18. [PubMed: 26832993]

17. Schultheis AM, Ng CK, De Filippo MR, Piscuoglio S, Macedo GS, Gatius S, et al. Massively Parallel Sequencing-Based Clonality Analysis of Synchronous Endometrioid Endometrial and Ovarian Carcinomas. J Natl Cancer Inst. 2016; 108

18. Dias-Santagata D, Akhavanfard S, David SS, Vernovsky K, Kuhlmann G, Boisvert SL, et al. Rapid targeted mutational analysis of human tumours: a clinical platform to guide personalized cancer medicine. EMBO Mol Med. 2010; 2:146–58. [PubMed: 20432502]

19. Assenov Y, Muller F, Lutsik P, Walter J, Lengauer T, Bock C. Comprehensive analysis of DNA methylation data with RnBeads. Nat Methods. 2014; 11:1138–40. [PubMed: 25262207]

20. Piscuoglio S, Ng CK, Martelotto LG, Eberle CA, Cowell CF, Natrajan R, et al. Integrative genomic and transcriptomic characterization of papillary carcinomas of the breast. Mol Oncol. 2014; 8:1588–602. [PubMed: 25041824]

21. Sahm F, Capper D, Pusch S, Balss J, Koch A, Langhans CD, et al. Detection of 2-hydroxyglutarate in formalin-fixed paraffin-embedded glioma specimens by gas chromatography/mass spectrometry. Brain Pathol. 2012; 22:26–31. [PubMed: 21631627]

22. Balss J, Pusch S, Beck AC, Herold-Mende C, Kramer A, Thiede C, et al. Enzymatic assay for quantitative analysis of (D)-2-hydroxyglutarate. Acta Neuropathol. 2012; 124:883–91. [PubMed: 23117877]

23. Debnath J, Brugge JS. Modelling glandular epithelial cancers in three-dimensional cultures. Nat Rev Cancer. 2005; 5:675–88. [PubMed: 16148884]

24. Debnath J, Muthuswamy SK, Brugge JS. Morphogenesis and oncogenesis of MCF-10A mammary epithelial acini grown in three-dimensional basement membrane cultures. Methods. 2003; 30:256–68. [PubMed: 12798140]

25. Someya S, Yu W, Hallows WC, Xu J, Vann JM, Leeuwenburgh C, et al. Sirt3 mediates reduction of oxidative damage and prevention of age-related hearing loss under caloric restriction. Cell. 2010; 143:802–12. [PubMed: 21094524]

26. Yang H, Ye D, Guan KL, Xiong Y. IDH1 and IDH2 mutations in tumorigenesis: mechanistic insights and clinical perspectives. Clin Cancer Res. 2012; 18:5562–71. [PubMed: 23071358]

27. Ko M, An J, Pastor WA, Koralov SB, Rajewsky K, Rao A. TET proteins and 5-methylcytosine oxidation in hematological cancers. Immunol Rev. 2015; 263:6–21. [PubMed: 25510268]

28. Gao J, Aksoy BA, Dogrusoz U, Dresdner G, Gross B, Sumer SO, et al. Integrative analysis of complex cancer genomics and clinical profiles using the cBioPortal. Sci Signal. 2013; 6:pl1. [PubMed: 23550210]

29. Ashworth A, Lord CJ, Reis-Filho JS. Genetic interactions in cancer progression and treatment. Cell. 2011; 145:30–8. [PubMed: 21458666]

30. Figueroa ME, Abdel-Wahab O, Lu C, Ward PS, Patel J, Shih A, et al. Leukemic IDH1 and IDH2 mutations result in a hypermethylation phenotype, disrupt TET2 function, and impair hematopoietic differentiation. Cancer Cell. 2010; 18:553–67. [PubMed: 21130701]

31. Lu C, Ward PS, Kapoor GS, Rohle D, Turcan S, Abdel-Wahab O, et al. IDH mutation impairs histone demethylation and results in a block to cell differentiation. Nature. 2012; 483:474–8. [PubMed: 22343901]

32. Turcan S, Rohle D, Goenka A, Walsh LA, Fang F, Yilmaz E, et al. IDH1 mutation is sufficient to establish the glioma hypermethylator phenotype. Nature. 2012; 483:479–83. [PubMed: 22343889]

33. Dang L, White DW, Gross S, Bennett BD, Bittinger MA, Driggers EM, et al. Cancer-associated IDH1 mutations produce 2-hydroxyglutarate. Nature. 2009; 462:739–44. [PubMed: 19935646]

34. Ward PS, Patel J, Wise DR, Abdel-Wahab O, Bennett BD, Coller HA, et al. The common feature of leukemia-associated IDH1 and IDH2 mutations is a neomorphic enzyme activity converting alpha-ketoglutarate to 2-hydroxyglutarate. Cancer Cell. 2010; 17:225–34. [PubMed: 20171147]

35. Kernytsky A, Wang F, Hansen E, Schalm S, Straley K, Gliser C, et al. IDH2 mutation-induced histone and DNA hypermethylation is progressively reversed by small-molecule inhibition. Blood. 2015; 125:296–303. [PubMed: 25398940]

36. Parsons DW, Jones S, Zhang X, Lin JC, Leary RJ, Angenendt P, et al. An integrated genomic analysis of human glioblastoma multiforme. Science. 2008; 321:1807–12. [PubMed: 18772396]

37. Yan H, Parsons DW, Jin G, McLendon R, Rasheed BA, Yuan W, et al. IDH1 and IDH2 mutations in gliomas. N Engl J Med. 2009; 360:765–73. [PubMed: 19228619]

38. Mardis ER, Ding L, Dooling DJ, Larson DE, McLellan MD, Chen K, et al. Recurring mutations found by sequencing an acute myeloid leukemia genome. N Engl J Med. 2009; 361:1058–66. [PubMed: 19657110]

39. Amary MF, Bacsi K, Maggiani F, Damato S, Halai D, Berisha F, et al. IDH1 and IDH2 mutations are frequent events in central chondrosarcoma and central and periosteal chondromas but not in other mesenchymal tumours. J Pathol. 2011; 224:334–43. [PubMed: 21598255]

40. Pansuriya TC, van Eijk R, d'Adamo P, van Ruler MA, Kuijjer ML, Oosting J, et al. Somatic mosaic IDH1 and IDH2 mutations are associated with enchondroma and spindle cell hemangioma in Ollier disease and Maffucci syndrome. Nat Genet. 2011; 43:1256–61. [PubMed: 22057234]

41. Itsumi M, Inoue S, Elia AJ, Murakami K, Sasaki M, Lind EF, et al. Idh1 protects murine hepatocytes from endotoxin-induced oxidative stress by regulating the intracellular NADP(+)/NADPH ratio. Cell Death Differ. 2015; 22:1837–45. [PubMed: 25882048]

42. Bose R, Kavuri SM, Searleman AC, Shen W, Shen D, Koboldt DC, et al. Activating HER2 mutations in HER2 gene amplification negative breast cancer. Cancer Discov. 2013; 3:224–37. [PubMed: 23220880]

43. Dang L, Yen K, Attar EC. IDH mutations in cancer and progress toward development of targeted therapeutics. Ann Oncol. 2016; 27:599–608. [PubMed: 27005468]

44. Cancer Genome Atlas Network. Comprehensive molecular portraits of human breast tumours. Nature. 2012; 490:61–70. [PubMed: 23000897]

45. Xu W, Yang H, Liu Y, Yang Y, Wang P, Kim SH, et al. Oncometabolite 2-hydroxyglutarate is a competitive inhibitor of alpha-ketoglutarate-dependent dioxygenases. Cancer Cell. 2011; 19:17–30. [PubMed: 21251613]

46. Fathi AT, Sadrzadeh H, Comander AH, Higgins MJ, Bardia A, Perry A, et al. Isocitrate dehydrogenase 1 (IDH1) mutation in breast adenocarcinoma is associated with elevated levels of serum and urine 2-hydroxyglutarate. Oncologist. 2014; 19:602–7. [PubMed: 24760710]

47. Sullivan LB, Chandel NS. Mitochondrial reactive oxygen species and cancer. Cancer Metab. 2014; 2:17. [PubMed: 25671107]

48. Stein EM. Molecular Pathways: IDH2 Mutations-Co-opting Cellular Metabolism for Malignant Transformation. Clin Cancer Res. 2016; 22:16–9. [PubMed: 26553750]
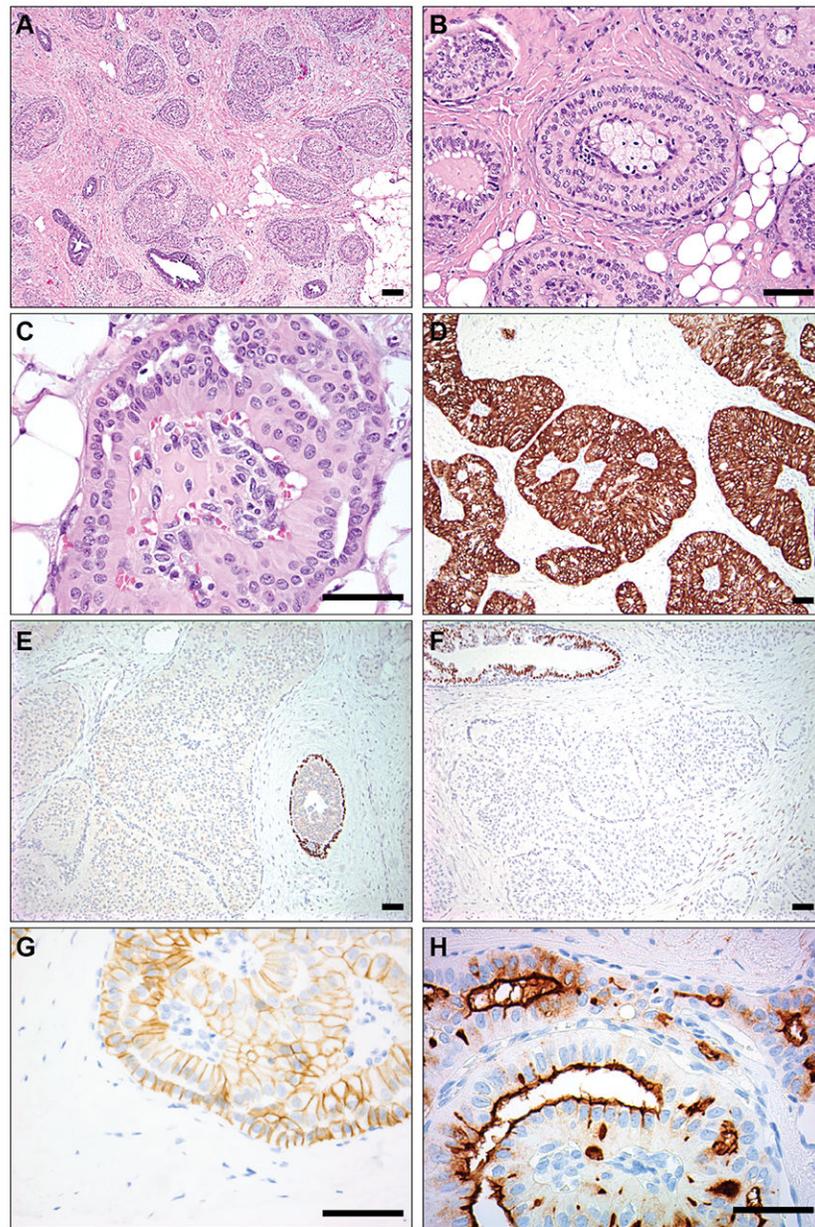
Figure 1. Histologic features and immunophenotype of SPCRP
(A) Circumscribed, solid papillary tumor cell nests infiltrating around and between normal ducts. (B) Solid papillary nests with fibrovascular cores containing aggregates of foamy histiocytes. (C) Columnar cells with abundant eosinophilic cytoplasm, mild nuclear atypia, and striking reverse nuclear polarity. (D) Neoplastic epithelium demonstrating diffuse and strong expression of high molecular weight cytokeratin CK5/6. (E) Absence of myoepithelial cells around tumor nests (left) on p63 immunostain with positive internal control (right). (F) Absence of ER staining with positive internal control (upper left). (G) Absence of apical and basal E-cadherin staining with preservation of lateral membrane expression. (H) Strong expression of MUC1 in apical membranes. Scale bars, 150μm.
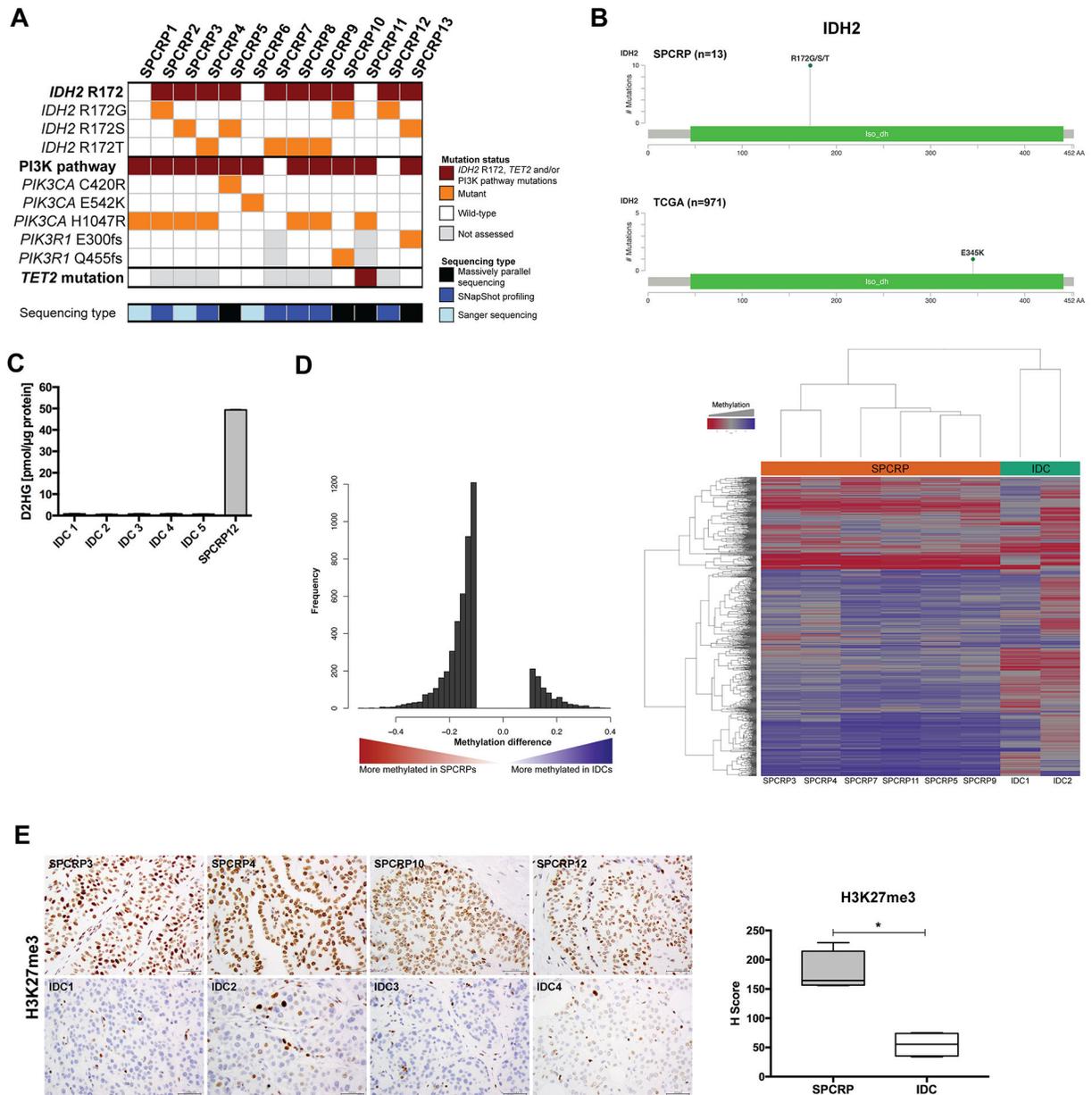
Figure 2. *IDH2* and PI3K pathway mutations, 2HG levels and methylation profiles of SPCRP
(A) Non-synonymous somatic *IDH2*, *TET2*, *PIK3CA*, and *PIK3R1* mutations identified in the 13 SPCRPs studied here by massively parallel sequencing (WES or MSK-IMPACT), SNaPshot or Sanger sequencing. (B) Mutation plot shows the domain structure of *IDH2* and the non-synonymous *IDH2* mutations identified in SPCRP and in common forms of breast cancer published by TCGA available from cBioPortal (28). (C) 2HG analysis in *IDH2*-mutant SPCRP (case 12) and IDH wild-type invasive ductal carcinoma of no special type (IDC). (D) *IDH2*/*TET2*-mutant SPCRPs display global DNA hypermethylation assessed by Infinium MethylationEPIC BeadChip as compared to *IDH2*/*TET2* wild-type IDCs (left). Unsupervised hierarchical clustering using all methylation values/ genes of six *IDH2*/*TET2*-mutant SPCRPs and two *IDH2*/*TET2* wild-type IDCs using complete linkage and Euclidean

distance (right). The 1000 genes with the highest variance across samples are displayed. Methylation status is color coded according to the legend. (E) H3K27me3 immunohistochemical analysis of four *IDH2*-mutant SPCRPs (top row) and four *IDH2* wild-type IDCs (bottom row). Nuclear immunoreactivity for H3K27me3 was quantified using the H-score. *, p<0.05; Mann-Whitney U test.

Figure 3. Downstream effects of IDH2 expression in nonmalignant breast epithelial cells
(A) Detection of 2HG as a readout of IDH2^{WT} and IDH2^{R172S} enzymatic activity in total protein lysates (left) and in conditioned media (right) of MCF10A^P and MCF10A^{H1047R} cells expressing empty vector control, IDH2^{WT} or IDH2^{R172S}. The same cell lysates from MCF10A^P and MCF10A^{H1047R} cells were analyzed for IDH2 protein expression by western blotting. Total tubulin was used as loading control; ns: not significant; ***P<0.001; ****P<0.0001; error bars represent standard deviation of mean. (B) Whole cell lysates of MCF10A^P and MCF10A^{H1047R} cells were analyzed for IDH2, total and phosphorylated RB, E-cadherin, and tubulin protein expression by western blotting (left), and quantified using near-infrared detection (LI-COR; Odyssey) (right); error bars represent standard deviation of mean.
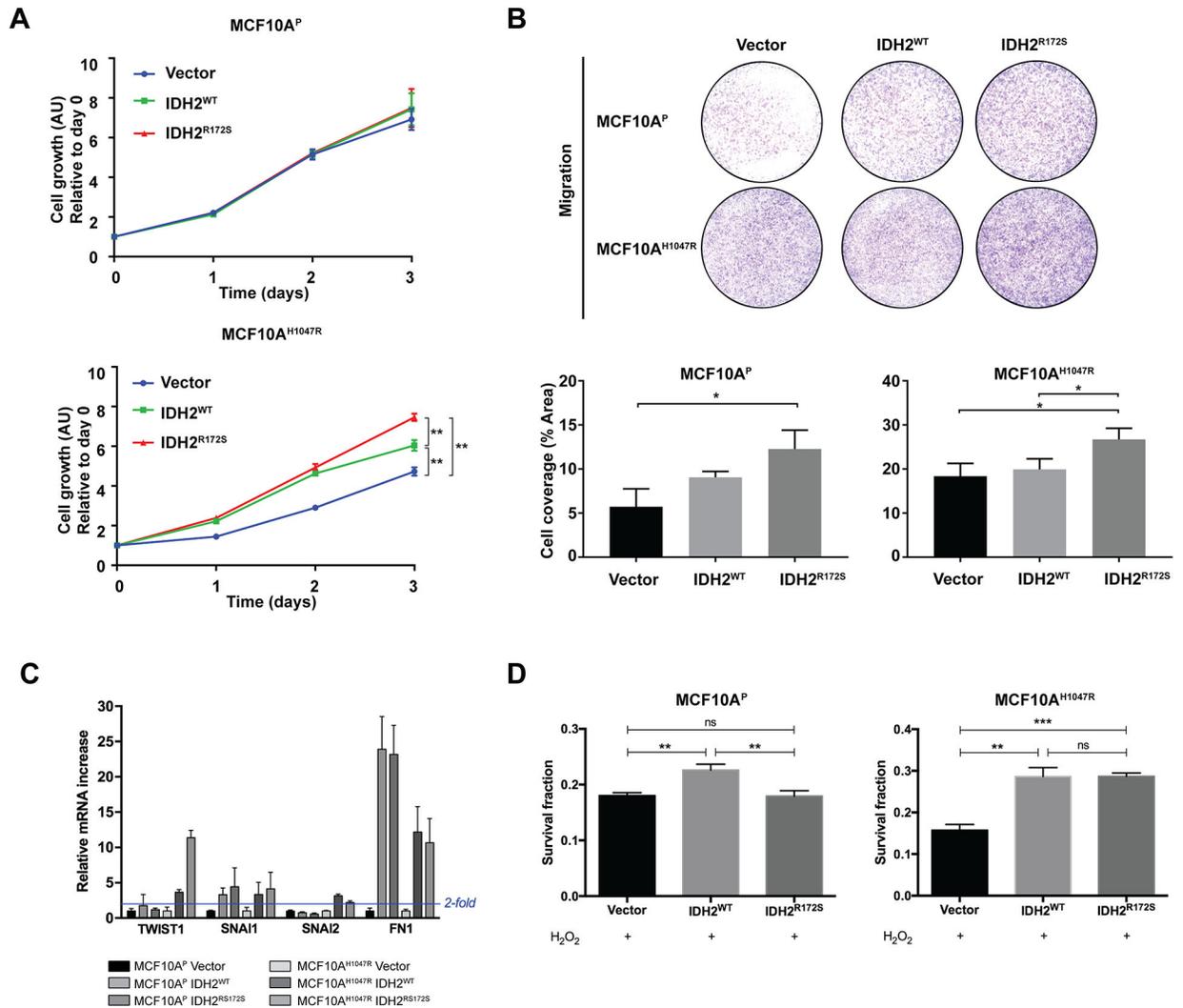
Figure 4. Effects of *IDH2* on proliferation, migration, mesenchymal marker expression and oxidative stress in non-malignant breast epithelial cells

(A) Effect of empty vector control (blue), IDH2^{WT} (green) or IDH2^{R172S} (red) expression on survival and growth of MCF10A^P (top) and MCF-10A^{H1047R} (bottom) assessed by MTT assay. **p < 0.01; error bars represent standard deviation of mean. (B) Effect of empty vector control, IDH2^{WT} or IDH2^{R172S} expression on transwell migration of MCF10A^P (top) and MCF-10A^{H1047R} (bottom). **p < 0.05; error bars represent standard deviation of mean. (C) Relative transcript expression for mesenchymal markers in MCF10A^P and MCF10A^{H1047R} cells expressing empty vector control, IDH2^{WT} or IDH2^{R172S} as determined by qRT-PCR. Two-fold increase above empty vector control for each cell line was used as a cut point. (D) Effect of H$_2$O$_2$ treatment of MCF-10A^P and MCF10A^{H1047R} cells expressing empty vector control, IDH2^{WT} or IDH2^{R172S} on cell viability fraction assessed by MTT assay as compared to untreated control cells. **P<0.01, ***P<0.001; error bars represent standard deviation of mean.
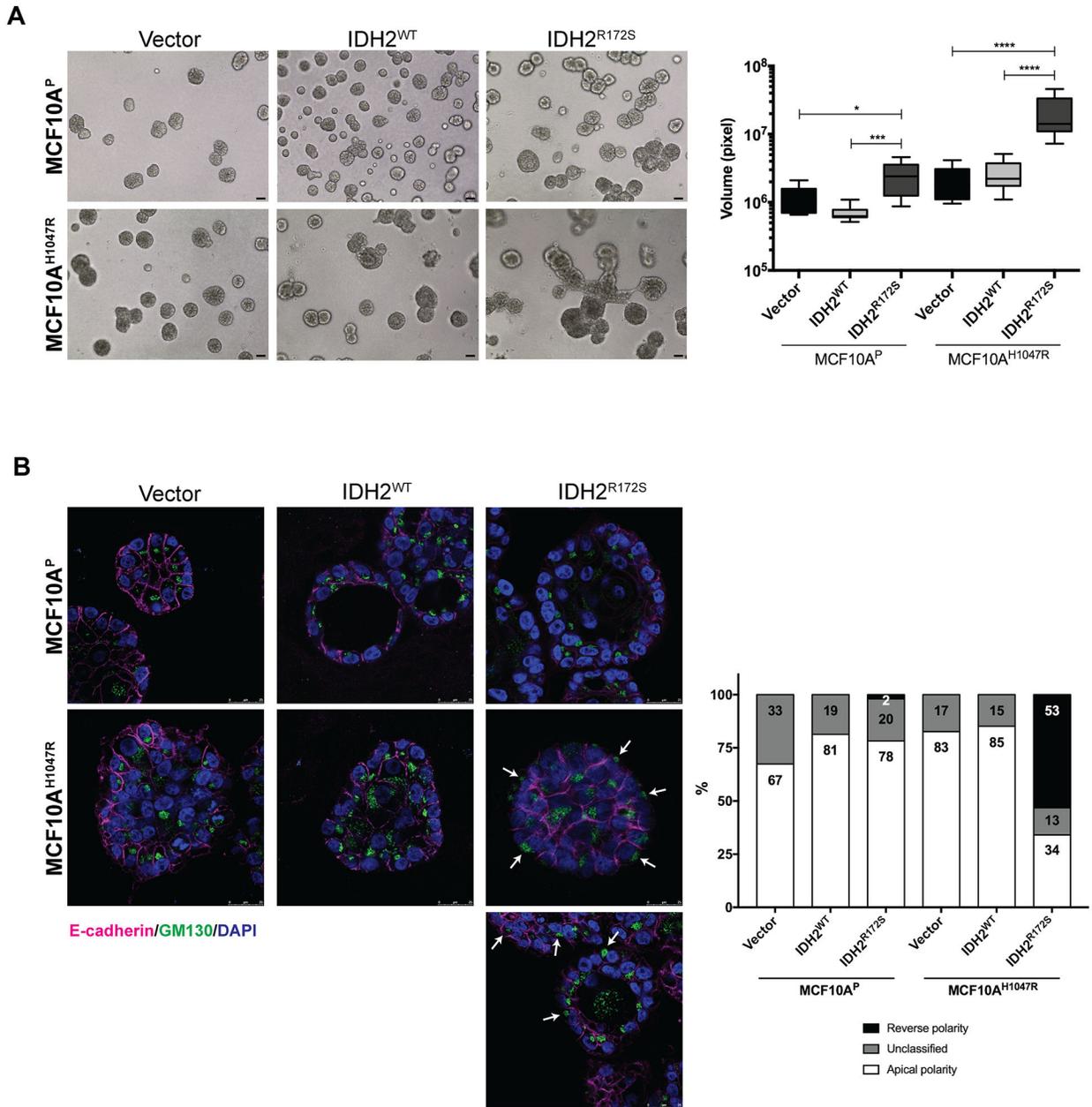
Figure 5. Impact of *IDH2* mutations on glandular architecture and polarity of non-malignant breast epithelial cells

(A) Impact of forced expression of IDH2^{WT} or IDH2^{R172S} on glandular architecture of MCF10A^P (top) and MCF10A^{H1047R} (bottom) cells grown in 3D basement membrane cultures (scale bar, 0.1 mm). The volume of the MCF10A^P and MCF10A^{H1047R} acinar structures expressing IDH2^{WT} and IDH2^{R172S} were quantified; *P<0.05; ***P<0.001; ****P<0.0001; error bars represent standard deviation of mean. (B) Immunofluorescent analysis of MCF10A^P and MCF10A^{H1047R} acinar structures expressing IDH2^{WT} or IDH2^{R172S} with antibodies against E-cadherin (red), cis-Golgi marker GM130 (green) and nucleus (DAPI, blue, scale bars, 25μm) (left). Arrows highlight cells with reverse polarity.

MCF10A^P and MCF10A^{H1047R} acinar structures showing either apical or reversed polarity were quantified. MCF10A^{H1047R} IDH2^{R172S} acini showed significantly more frequently inverted polarity than MCF10A^{H1047R} vector control and MCF10A^{H1047R} IDH2^{WT} acini (*$P<0.05$ each; t-test).

Table 1

Clinicopathologic characteristics of SPCRP analyzed in this study.

	1	2	3	4	5	6	7	8	9	10	11	12	13
Clinical findings													
Age, y	68	62	63	79	64	51	64	58	66	65	70	65	65
Laterality	L	L	L	R	R	R	L	R	R	L	L	L	L
Size, cm	0.9	0.8	1.2	U	1.8	0.8	1.4	0.6	0.9	1.5	1.3	1.2	0.9
LN metastasis/ sampled	U	0/2	NP	U	0/2	0/3	0/1	U	0/3	0/2	0/2	0/4	U
Outcome/mo	U	NED/77	U	U	NED/31	NED/30	NED/29	U	NED/20	NED/37	NED/12	U	U
Treatment	U	S/XRT	U	U	U	S	S/XRT	U	S/C	S/XRT/C	U	U	U
Cancer history	U	+	U	U	-	+	-	U	-	-	-	U	U
Immunohistochemical features													
CK5/6	+	+	+	+	+	+	Rare +	-	+	+	Focal +	Focal +	+
CK7	+	+	+	+	+	+	+	+	+	-	+	+	NP
CK 34βE12	NP	+	+	+	+	+	-	+	+	-	+	+	NP
CK AE1/AE3	NP	+	NP	+	+	NP	+	+	+	+	+	+	NP
p63	-	-	-	-	-	-	-	-	-	-	-	-	-
SMMHC	-	-	-	-	-	-	-	-	-	-	-	NP	-
Calponin	-	-	-	-	-	-	-	-	-	NP	-	-	NP
ER	-	-	<10% +	-	-	<10% +	<10% +	-	-	<10% +	<10% +	-	-
PR	-	-	<10% +	NP	-	<10% +	-	-	-	-	-	-	-
HER2	NP	-	NP	NP	-	-	-	-	-	-	-	-	-
AR	NP	-	-	-	-	-	-	-	-	NP	-	-	Focal +
GCDFP-15	Focal +	-	Focal +	Focal +	Focal +	Focal +	-	-	Focal +	-	Focal +	-	Focal +
Mammaglobin	Focal +	+	Focal +	Focal +	Focal +	-	-	-	-	-	Focal +	+	Focal +
TTF-1	-	-	NP	-	-	-	-	-	-	-	-	-	-
Thyroglobulin	NP	-	NP	-	-	NP	-	-	-	-	-	-	-

Abbreviations: AR, androgen receptor; C, chemotherapy (carboplatin and taxol); CK, cytokeratin; ER, estrogen receptor; GCDFP-15; gross cystic disease fluid protein-15; L, left; LN, lymph node; mo, months; NED, no evidence of disease; NP, not performed; R, right; SMMHC, smooth muscle myosin heavy chain; TTF-1, thyroid transcription factor-1; U, unknown; XRT, radiation; y, years